Supplementary Material

1 DEVICE DESIGN FABRICATION AND CHARACTERIZATION

In this section we describe the VECSEL design.

1/2 VCSEL design

The $1/2$-VCSEL (gas229) gain mirror structure (see Fig. S1(a)) used in this work is grown on a [001] GaAs doped substrate in a low pressure metal-organic-chemical-vapor-deposition in a D-180-Veeco TurboDisc reactor using TMGa, TMAI, TMIn, and AsH3 at 60 mTorr at a temperature of $700°C$. It contains a high reflectivity ($99.9\,\%$) $Al_{0.85}Ga_{0.15}As$/GaAs 27 pairs Distributed-Bragg-Reflector (DBR), and a $13\,\lambda/2$ thick active layer. It contains 6 strain-balanced InGaAs/GaAsP QWs emitting at $\lambda \simeq 1\,\mu$m and GaAs pump absorbing barriers. Strain compensation layers of GaAsP are included to avoid plastic relaxation of the active region structure. The two surrounding 280nm thick barriers are in GaAsP with $5\,\%$ of phosphore to compensate the QW strain ($\Delta a/a \simeq 1.3\%$). A low phosphore concentration is chosen to minimize the barrier height between GaAs and GaAsP at 300 K, for efficient capture of excited carriers in the QWs. Those QWs are located on optical standing-wave antinodes, with a 111010100100 distribution function from surface to Bragg such as the excited carrier density is almost equal in all QWs, using a QW carrier capture time of ~ 20 ps), to ensure a low laser threshold and a homogeneous gain. The active region is designed for efficient optical pumping in the thick GaAs barriers with a GaAs commercial diode laser emitting at 808 nm. The total pump absorption in the barriers is $\sim 87\%$ (absorption coefficient $\sim 1.2/\mu m$). On the top of the $13\,\lambda/2$ thick active layer an 30 nm AlAs confinement layer and then to avoid oxydation a 20 nm GaAs cap layer are grown. A close to $\lambda/4$ SiN thick coating is deposited on top surface to reduce micro-cavity resonance filtering effect on gain bandwidth. Fig. S1(b) shows the measured intensity reflectivity of the half VCSEL and the calculated second order dispersion (GDD) of the reflection phase. The calculated dispersion has been obtained by calculating the complex reflectivity spectrum of the sample structure with the transfer matrix formalism detailed in ref(Tropper and Hoogland, 2006) and obtaining the second derivative of the electric field's phase with respect to the wavelength.

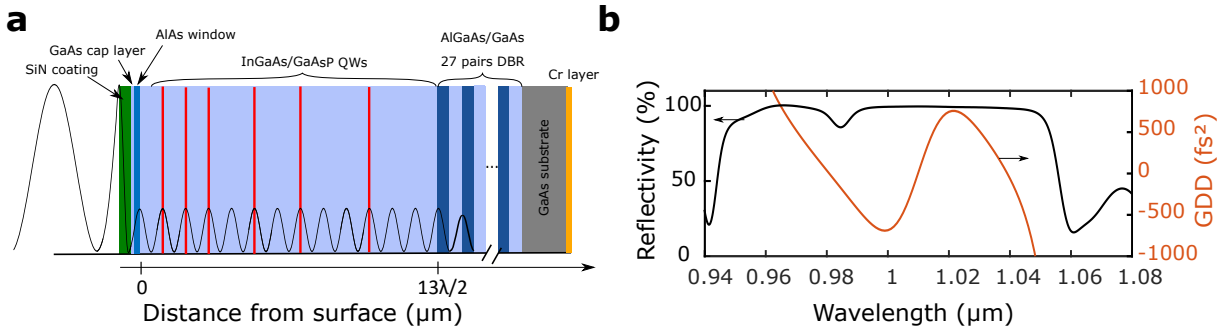

Figure S1. (a) Design of the half VCSEL and intensity of the electric field inside the structure. (b)Spectral dependence of the intensity reflectivity and second order dispersion of the half VCSEL.

This microcavity acts as a Gires-Tournois-Interferometer (GTI) and approximating its reflection phase by a Taylor expansion close to the laser operating angular frequency ω_0 leads to the dispersion parameters:

$$\Phi(\omega_0)_n = \frac{\partial^n}{\partial \omega^n} arg[\frac{-\sqrt{R_2} + \sqrt{R_1} e^{i\omega\tau}}{1 - \sqrt{R_1 R_2} e^{i\omega\tau}}]|_{\omega=\omega_0} \tag{S1}$$

The parameter R_1 describes the reflectivity of the DBR, R_2 is the reflectivity of the gain mirror's top surface, τ is the microcavity round trip time. Φ_1 corresponds to a time delay (the time photons are stored inside the microcavity), Φ_2 is the second order group delay dispersion (GDD) and Φ_3 is the third order group delay dispersion (TOD). Fig. S2 shows the different dispersion orders that correspond to the gain mirror used in this work using the parameters $R_1 = 1$, $R_2 = 0.0035$ and $\tau = 70\,\mathrm{fs}$.

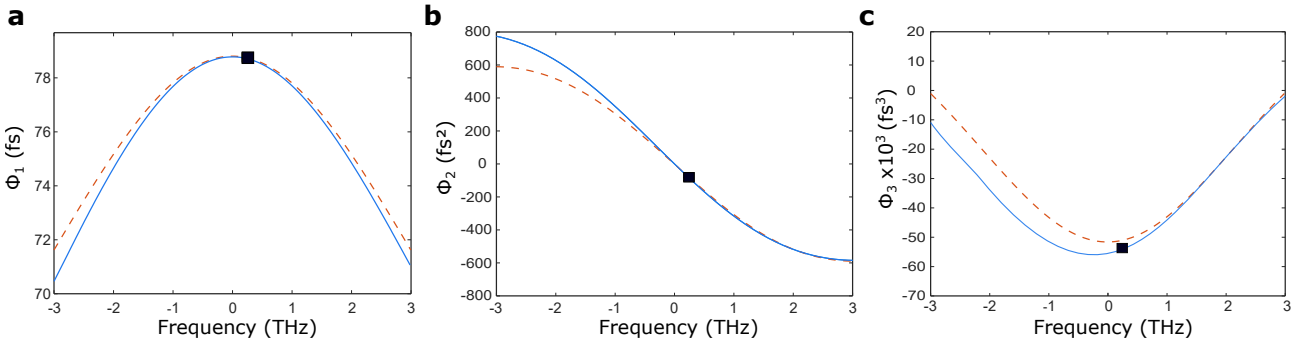

Figure S2. Phase dispersion of the half VCSEL obtained with the transfer matrix formalism (blue line) and corresponding GTI (red dashed line). (a) Time delay, (b) Group Delay Dispersion (GDD), and (c) Third Order Dispersion (TOD). The center frequency is the resonance frequency of the microcavity $\omega/2\pi = 296.9$ THz or $\lambda = 1.0105\ \mu m$. The laser is operating slightly off resonance and the corresponding value of the dispersion parameters are indicated by the black squares, $\Phi_1 = 78.7\,\mathrm{fs}$, $\Phi_2 = -80\,\mathrm{fs}^2$ and $\Phi_3 = -53\,000\,\mathrm{fs}^3$.

Optical cavity design and selection of a single light state

In this section we describe the laser cavity and show that the reported non-linear dynamics is solely due to degenerated four-wave mixing that couples the longitudinal modes.

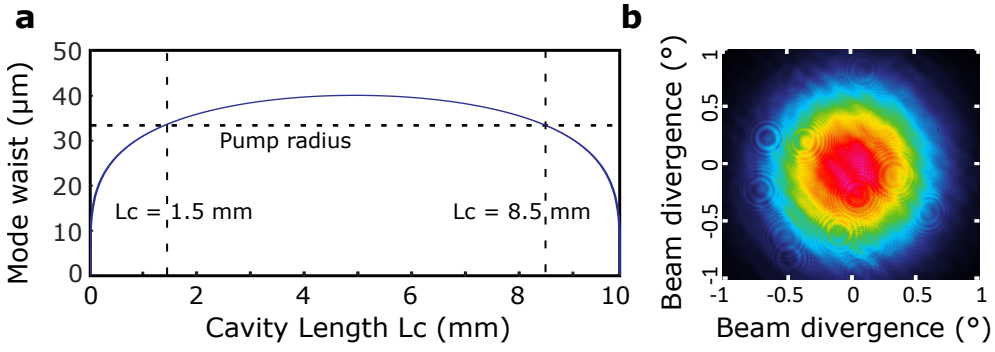

Figure S3. (a) Optical cavity stability. (b) Transverse beam far field profile.

The laser cavity includes the gain mirror (gas 229), an air gap and a commercial dielectric coated output coupler ($Rcc = 10\,\mathrm{mm}$, $Tr = 1\ \%$). The substrate back side of the gain mirror was polished with an angle

($\sim 2°$) to avoid parasitic Fabry-Perot fringes and backscattering from the substrate ($\sim 300\mu$m thick). The gain structure is temperature stabilized thanks to a Peltier thermoelectric cooler and optically pumped by a 808-nm 400 mW low noise single-mode diode laser (LD785-SE400) on a $\sim 30\,\mu$m radius (at $\sim 70\,°$ Brewster angle). The cavity length and the mirror radius of curvature are chosen so the waist of the TEM_{00} mode matches with the Gaussian pump radius to prevent high order transverse modes operation (Fig. S3(a)). In this work we have use two cavity lengths L_c that satisfies this condition, $L_c = 1.5\,\mathrm{mm}$ and $L_c = 8.5\,\mathrm{mm}$. The stabilized single fundamental Gaussian mode is shown in Fig. S3(b). The laser is operating at room temperature in continuous wave regime at a wavelength of $\lambda = 1.01\ \mu$m.

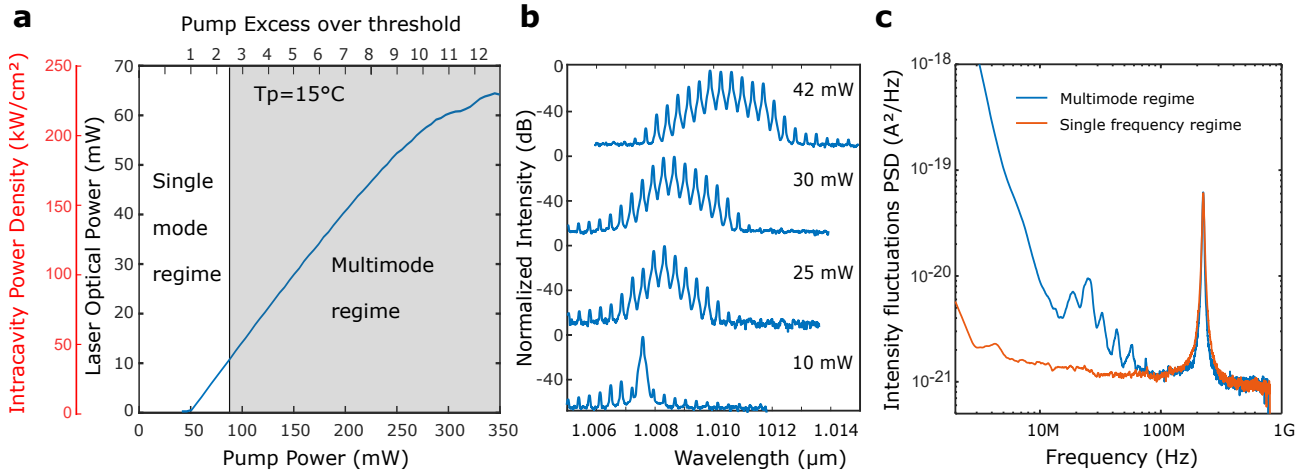

Figure S4. (a) Laser output power according to the pump power for a Peltier temperature T_p of $15°C$. The corresponding intracavity power density is also plotted. (b) High resolution $0.02\,\mathrm{nm}$ optical spectra for different output power. (c) RF spectrum of the beating between the two polarization modes in both single frequency (red curve) and multimode (blue curve) regime.

The laser beam is collimated using a 75 mm focal achromatic lens, followed by an optical isolator to prevent from parasitic feedback. The output power of the laser according to the pump power is shown in Fig. S4(a). The laser reaches threshold for a pumping power of $P_{th} = 50$ mW and achieve a maximum output power of 60 mW before roll over. The threshold density is around $1.8\,kW/cm^2$ which corresponds to twice the QWs transparency. Pump excess over laser threshold is then defined by : $\eta = (P_p - 0.5P_{th})/(P_{th} - 0.5P_{th})$ which ranges from 1 to 10 with P_p the optical power of the laser diode. Starting from threshold the laser emits a single frequency with a side mode suppression ratio better than 50 dB but oscillates in many modes for a pumping power starting at around 80 mW. Fig. S4(b) shows the laser optical spectra for different output power, revealing an increasing number of oscillating modes with pump power.

The device exhibits in-plane linearly polarized light along the [110] crystal axis of the gain mirror thanks to gain anisotropy in the quantum wells and birefringence in the semiconductor crystal (Garnache et al., 2007; Seghilani, 2015; Fördös et al., 2017) with a measured orthogonal polarization extinction ratio around 70 dB between the two non-degenerate states. The RF spectrum that shows the beating between the two polarization states at $\sim 220\,\mathrm{MHz}$ is shown in Fig. S4(c). To generate this beating, we used a linear polarizer oriented at 45° with respect to the crystal axis. In this condition, the beam is focused on a low noise detector and the noise spectrum of the laser is measured in the single frequency regime ($T_p = 15°$, $Pp = 70\,\mathrm{mM}$) and in the multimode regime ($T_p = 15°$, $Pp = 150\,\mathrm{mW}$). Attenuating the beam, the photocurrent at the output of the detector is kept at 1.2 mA in both cases. While the laser total output intensity strongly

fluctuates in the multimode regime (blue curve in Fig. S4(c)), the beating between the two polarization states does not change.

Thus, there is only one possible state with respect to transverse electric field and its polarization, and only remains for the laser a possible non linear dynamics between the longitudinal modes. Moreover, light and matter spatial inhomogeneity (non linear through longitudinal spatial hole burning and carrier diffusion in the gain region, and passive defects assisted diffusion) are suppressed thanks to delta-like distribution of QW gain layers located on one end mirror in this empty-like cavity ($\leq 0.1\ \%$ longitudinal filling factor; $\sim 100\ \%$ transversally). The only residual effect of relatively large QW number ($\simeq 6-12$) on axis spatial distribution - on E-field nodes -, is to create a spectrally broadband filtering (much larger than γ here). This leaves only coherent temporal non-linear dynamic phenomena, and prevent from complex or chaotic behaviors. In addition, QW intraband carrier dynamics - spectral hole burning and carrier heating - are too fast ($\ll 1ps$) compared to the fastest time scale and can be neglected. Thus the only non-linear remaining force that can drive the system unstable is degenerated four-wave mixing occurring under light-matter interaction process in the gain due to population pulsation at the cavity free-spectral-range pulsation $\Delta\omega = 2\pi/T$, where T is the cavity round-trip time. This is a great advantage compared to Fabry-Perot diode laser, solid state laser, or ring microresonator laser.

2 EXPERIMENTAL TOOLS FOR THE LASER MULTIMODE DYNAMICS CHARACTERIZATION

Multimode dynamics of the device was investigating by recording the cw optical spectrum at the output of a 25 GHz (or 14 GHz using the second order diffraction) resolution grating monochromator (JY HR1000), using a streak camera (Hamamatsu C10910-02) with a time resolution of 200 ns. The total intensity output fluctuations of the laser is also recorded with a low noise photodiode on a 2 GHz bandwidth.

Laser dynamics at the cavity round-trip frequency ($\sim 100\,\mathrm{GHz}$ here) was first investigated by detecting the second-harmonic generated (SHG) signal though a rapid scanning autocorrelator (FR-103XL) on a $150\,\mathrm{ps}$ of delay. Secondly the beating between the different longitudinal modes in the laser intensity was investigated by excitation of a commercial unitraveling-carrier photodiode (IOD-PMAN-13001-1 from NTT). This photomixer module has an integrated broadband-type planar antenna. The 100 GHz output is extracted in free space from the photomixer using a high-resistivity Si lens, thus offering a lower output power but a wider bandwidth, in comparison to photomixers integrated in rectangle metallic waveguides. The microwave signal that comes from the photodiode is collimated using a 10-cm focal-length Teflon lens, then focused using an identical lens into a commercial heterodyne receiver (RPG SAR-110) operating in the 75-110 GHz range with an input pyramidal horn antenna (SAR-2309-10-S2). This receiver is an active frequency down converter driven by a RF spectrum analyzer (Rohde and Schwarz FSV), thus offering a high signal-to-noise ratio (noise floor of -60 dBm at 75 GHz to -85 dBm at 110 GHz for video and resolution bandwidths of 1 MHz). Thanks to a provided conversion losses table, the RF power can be directly measured using the spectrum analyzer.

3 IMPACT OF THE TOD ONTO THE LASER DYNAMICS

The laser is operated close to the resonance of the 1/2 VCSEL microcavity to introduce a desirable amount of dispersion (see Fig. S2). Yet, close to resonance the second-order dispersion is small and the third-order contribution becomes dominant. In this section we investigate the impact of the term Φ_3 in Eq. (1) of

the main text onto the comb stability. This consideration would provide guidance for the engineering of dispersive effects in the 1/2 VCSEL structure.

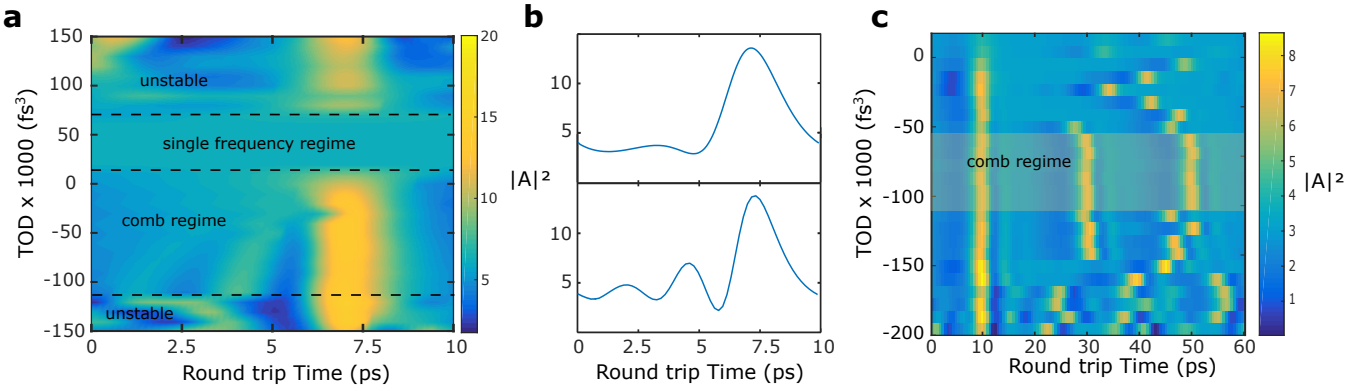

Figure S5. (a)Pulse profile in the short cavity configuration ($L_c = 1.5\,\mathrm{mm}$) as Φ_3 is varied for parameters ($1 \times 10^9\ s^{-1}$, $2.8 \times 10^{13}\ s^{-1}$,10 ps, 0.01, 2, 8, 90 fs, $-80\,\mathrm{fs}^2$). (b) Pulse profile for $\Phi_3 = 0 f s^3$ (top) and $\Phi_3 = -10^5 f s^3$ (bottom).(c) Pulse profile in the long cavity configuration ($L_c = 8.5\,\mathrm{mm}$) as Φ_3 is varied for parameters ($1 \times 10^9\ s^{-1}$, $2.8 \times 10^{13}\ s^{-1}$,60 ps, 0.01, 2, 4, 80 fs, $-60\,\mathrm{fs}^2$).

Fig. S5(a) shows the pulse intensity in the cavity for second order dispersion $\Phi_2 = -80\,\mathrm{fs}^2$ in the short cavity configuration ($L_c = 1.5\,\mathrm{mm}$) where a single pulse only travels in the cavity. As the value of TOD is varied we observed that the comb regime is obtained only for a bounded range of TOD ($[-110\,000\,\mathrm{fs}^3; 10\,000\,\mathrm{fs}^3]$). Strong values of TOD results in a comb instability. Furthermore this range is clearly asymmetric with the sign of TOD and a pulse is stabilized mainly for negative values. This has direct consequences for the design of the microcavity VCSEL where an antiresonant structure, rather than a resonant one, introduces a positive amount of TOD in the vicinity of zero GDD. In the range of TOD where a comb regime is found one can see that oscillations in the leading tail preceding the main pulse develops as negative TOD is increased (Fig. S5(b)). In the long cavity configuration ($L_c = 8.5\,\mathrm{mm}$) a regime of harmonic mode locking takes place and three pulses travel in the cavity as seen in Fig. S5(c). However in this case, a non zero value of negative TOD is necessary to stabilize a comb regime.

REFERENCES

Tropper A, Hoogland S. Extended cavity surface-emitting semiconductor lasers. *Progress in Quantum Electronics* **30** (2006) 1–43. doi:https://doi.org/10.1016/j.pquantelec.2005.10.002.

Garnache A, Ouvrard A, Romanini D. Single–Frequency operation of External–Cavity VCSELs: Non-linear multimode temporal dynamics and quantum limit. *Optics Express* **15** (2007) 9403–9417.

Seghilani MS. *Highly coherent III-V-semiconductor laser emitting phase-, amplitude- and polarization-structured light for advanced sensing applications : Vortex, SPIN, Feedback Dynamics.*. Ph.D. thesis, Université Montpellier (2015). doi:NNT:2015MONTS207.tel-02049651.

Fördös T, Jaffrès H, Postava K, Seghilani MS, Garnache A, Pištora J, et al. Eigenmodes of spin vertical-cavity surface-emitting lasers with local linear birefringence and gain dichroism. *Phys. Rev. A* **96** (2017) 043828. doi:10.1103/PhysRevA.96.043828.